

Maximal Interaction of Electromagnetic Radiation with Corona-Virions

Constantinos Valagiannopoulos^{1, a)} and Ari Sihvola^{2, b)}

¹⁾*School of Sciences and Humanities, Nazarbayev University, KZ-010000, Kazakhstan*

²⁾*School of Electrical Engineering, Aalto University, FI-00076, Finland*

(Dated: 28 July 2020)

Absorption and scattering of the impinging electromagnetic waves are the two fundamental operations describing the energy exchange of any, organic or inorganic, particle with its environment. In the case of virion cells, substantial extinction power, counting both absorbing and scattering effects, is a prerequisite for performing a variety of coupling actions against the viral particles and, thus, a highly sought-after feature. By considering realistic dispersion for the dielectric permittivity of proteins and a core-shell modeling allowing for rigorous formulation via Mie theory, we report optical extinction resonances for corona-virions at mid-infrared range that are not significantly perturbed by changes in the objects size or the background host. Our findings indicate the optimal regime for interaction of photonic radiation with viral particles and may assist towards the development of equipment for thermal damage, disintegration or neutralization of coronavirus cells.

I. INTRODUCTORY COMMENT

The energy exchange between an impinging light beam and virus particles is a cornerstone in several biophotonic operations with important applications in Microbiology, Pharmacology, Medical Physics and Biochemistry. The study of this interaction between virions and electromagnetic fields has been greatly assisted by a large set of analytical methods and physical concepts reported for inorganic particles¹. That inevitably led in their implementation and translation to understand how microbes absorb and re-emit visible light in various directions² or what are the biophysical processes behind ultraviolet germicidal irradiation³. Furthermore, applications of diverse types of scattering techniques to systems of microorganisms have been reviewed⁴ while the diffusion behavior of viral macromolecules into liquids has been extensively elaborated⁵. Importantly, highly sensitive virus detection has become possible based on optical trapping⁶ or via the reactive shift of a whispering-gallery mode⁷, facilitating convenient medical diagnosis and food inspection. In addition, the coupling of the incident beams with virions has been utilized in measuring the refractive index of the cells with high precision⁸ and analyzing single viruses with a resolution comparable to that of electron microscopy⁹.

Mie theory¹⁰, admitting rigorous solution to the scattering of electromagnetic waves by multilayered spheres, makes a powerful tool for treating similar problems involving radiation impinging on virus particles, due to their quasi-spherical shapes. In particular, simple formulas are derived towards the interpretation of the characteristic anomalies in the optical activity of membrane suspensions¹¹ or for the evaluation of collective backscattering from abundant viruses into sea water¹². Mie scattering has been also used to model the light intensity produced by virion-like nano-objects in biosensors¹³, flow cytometers¹⁴ and phase microscopes setups¹⁵. Finally, analytical expressions have been provided for the shifts in the resonance frequencies of spherical dielectric microresonators ow-

ing to plasmonic nanoparticles¹⁶ or protein binding¹⁷, paving the way to highly-efficient bioimaging.

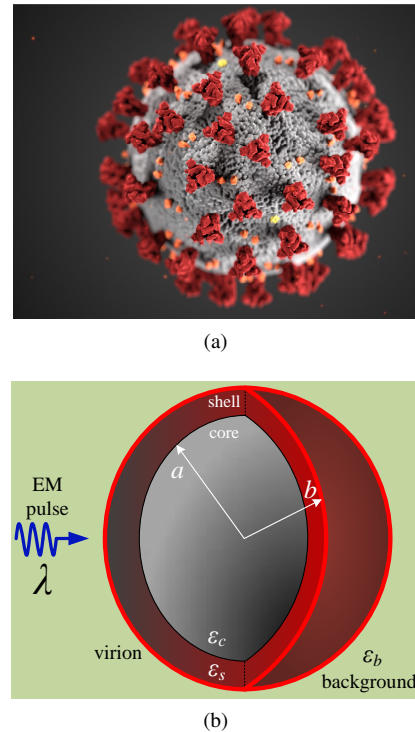


FIG. 1. (a) Illustrative representation revealing the coronavirus morphology when viewed via electron microscope. Both the gray core and the brown spikes, that adorn the outer surface of the virus imparting the look of a corona surrounding the virion, are made of proteins. The image has taken from Public Health Image Library (PHIL) and is free of any copyright restrictions. (b) The adopted model in the present study; the spikes are replaced by an isotropic shell of permittivity ϵ_s and thickness $(b - a)$ surrounding a homogeneous core of permittivity ϵ_c and radius a ; the structure is hosted by a background medium of permittivity ϵ_b . The virion is bombarded by an electromagnetic (EM) pulse of high intensity and central wavelength λ .

^{a)}Electronic mail: konstantinos.valagiannopoulos@nu.edu.kz

^{b)}Electronic mail: ari.sihvola@aalto.fi

Coronaviruses constitute a special category of viruses whose genome is hosted into protein cells, with rod-shaped spikes projecting from their surfaces; these elongated bumps,

when seen through electron microscope, create an image mimicking the solar corona, to which the viruses owe their name. Since the 2020 global pandemic outbreak^{18,19}, the whole world became familiar with the term “coronavirus” while medical scientists struggle to handle²⁰ that continued threat, responsible for hundreds of thousands of deaths and unprecedented socio-economic damage. Due to the alarming situation, numerous experimental efforts have been devoted to test the photonic response of that specific coronavirus (SARS-CoV-2) for various objectives like the fast biosensing that secures reliable viral disease diagnosis²¹ or the development of cellular nanosponges that are allegedly able to neutralize the virus²². Interestingly, several studies also indicate that phototherapy has immense potential to reduce the impact of coronavirus diseases²³, and offers suggested ways that the health-care industry can integrate modern light technologies in the fight against SARS-CoV-2 and its mutant versions.

However, analytical modeling via Mie theory is very rarely²⁴ involved to works studying the light-coronavirus interactions, despite its rigorous yet simple formulation. In this paper, we systematically examine the Mie scattering of a protein nanosphere covered by a suitably homogenized shell emulating the presence of amine radial spikes. The size of the core²⁵ and the spikes length²⁶ are varying between their realistic limits, according to the adopted conceptual layouts²⁶ and the images taken from electron microscopes²⁷. As far as the background media that host the virions are concerned, they are also selected based on the presently available data, since the virus can transmit through the air²⁸, while can exist into blood²⁹ and the human organs like liver³⁰ as well. The impinging electromagnetic pulse is harmonic with frequency that spans from the hard ultraviolet to the long infrared part of the spectrum; the dispersion of the incorporated materials across this extensive band is taken into account, based on experimental measurements contained in well-established references^{31–33}. Our aim is to maximize the extinction power from the core-shell nanoparticle, which is a prerequisite for any action against the virion from disintegration to isolation. The influence of the geometric characteristics of the considered model on the observable quantity is identified and the optimal mid-infrared wavelengths leading to substantial extinction are determined. Importantly, the reported resonances are found highly insensitive to structural changes regardless of the background and thus are applicable to ensembles of corona-virions of diverse features. Our findings may inspire clinical research towards the development of diagnostic products and devices that require significant power interaction with SARS-CoV-2 particles to dissolve or neutralize them.

II. PROPOSED APPROACH

A. Core-Shell Model

As shown in the illustrative sketch of Fig. 1(a), a typical corona-virion is composed of a homogeneous core (nucleocapsid), containing a mixture of proteins²⁵, surrounded by radial spikes of glycoprotein³⁴. We treat all proteins as diiso-

propylamine, also known as DIPA, whose dispersive permittivity $\epsilon_c = \epsilon_c(\lambda)$ can be easily found. As far as the crown of protein rods is concerned, the simplest way to model it is as a homogeneous shell of permittivity given by a weighed sum of the protein dielectric constant ϵ_c and that of the background medium ϵ_b :

$$\epsilon_s = (1-s)\epsilon_b + s\epsilon_c, \quad (1)$$

where $0 < s < 1$ is the filling factor indicating the percentage of the corona volume occupied by the spikes.

We could follow alternative and more accurate approaches to model the photonic setup of the virion, like approximating the shell by quasi-homogeneous multilayers³⁵, considering radial anisotropy^{36,37} or even assuming systropic properties for the fabric of the spherical particles³⁸. In this case, the scalar ϵ_s would have been replaced by a uniaxial tensor $[\epsilon_s] = \text{diag}(\epsilon_r, \epsilon_t, \epsilon_t)$ in spherical coordinates (r, θ, φ) . The radial permittivity $\epsilon_r = \epsilon_s$ will be given by (1) since the corresponding depolarization factor of a needle vanishes. On the contrary, the transversal constant (along local θ, φ directions), ϵ_t , will be written as³⁹:

$$\epsilon_t = \epsilon_b \frac{(\epsilon_b + \epsilon_c) - s(\epsilon_b - \epsilon_c)}{(\epsilon_b + \epsilon_c) + s(\epsilon_b - \epsilon_c)}. \quad (2)$$

The solution of the wave equation into such a medium involves cylindrical Bessel functions J_ν, Y_ν of orders⁴⁰:

$$\nu = \nu_n = \frac{1}{2} \sqrt{1 + 4 \frac{\epsilon_t}{\epsilon_r} n(n+1)}, \quad (3)$$

for $n \in \mathbb{N}^*$.

However, the size of the virion is small (average radius $b \cong 60$ nm) and the regarded wavelengths large (average $\lambda \cong 3500$ nm, mid-infrared); accordingly, the incoming beams are not expected to “feel” a more advanced setup emphasizing on the geometry details. In other words, a very slowly moving wave will perceive the very complicated actual structure of the protein spikes in the same way as a homogeneous cladding of texture determined by (1). Thus, we advocate that the model in 1(b), where the core (permittivity ϵ_c) of radius a is engulfed by the shell (permittivity ϵ_s) of size $(b-a)$ and host into a homogeneous background (permittivity ϵ_b), captures sufficiently the electromagnetic interactions and the underlying photonic power interplay between the incident fields and the particle. Note finally that the Bessel order (3) becomes complex if the permittivities (1),(2) have non-zero imaginary parts, which is the case in our consideration; as a result, numerical issues⁴¹ may emerge if the shell is assumed anisotropic. That makes an extra reason to follow the isotropic and homogeneous modeling via (1).

B. Mie-Theory Formulation

We assume that the virion of Fig. 1(b) is illuminated by an electromagnetic beam in the form of monochromatic plane wave (with free-space oscillating wavelength $\lambda \equiv 2\pi/k_0$), traveling into the background host. As mentioned above, the

symbols (r, θ, φ) are used for the related spherical coordinates centralized at the cell, while the equivalent Cartesian ones read (x, y, z) ; the suppressed harmonic time is of the form $e^{+i2\pi ct/\lambda}$, where c is the speed of light into free space. For simplicity and without loss of generality (due to the spherical symmetry), we assume that the incident wave propagates along $+z$ axis and its electric field vector is always parallel to x axis oscillating with amplitude $E_0 > 0$ (measured in *Volt/meter*). This background field can be decoupled in two terms, each of which satisfies Maxwell's laws: one term with no radial electric component (TE) and another one with no radial magnetic component (TM). These terms can be expressed as series of spherical harmonics, which dictate the θ - and φ -dependence of the field quantities in all the regions defined by the concentric and entire surfaces, according to the rigorous Mie theory¹⁰.

After imposing the necessary boundary conditions, the scattered fields for $r > b$ (electric field vector of TE set and magnetic one for TM set), are written as⁴²:

$$\mathbf{E}_{scat}^{TE} = E_0 \sum_{n=1}^{+\infty} i^{-n} S_n^{TE} h_n(k_b r) \left\{ \begin{array}{l} -\hat{\theta} \csc \theta p_n(\theta) \cos \varphi \\ +\hat{\phi} p_n'(\theta) \sin \varphi \end{array} \right\},$$

$$\mathbf{H}_{scat}^{TM} = \frac{E_0 \sqrt{\epsilon_b}}{\eta_0} \sum_{n=1}^{+\infty} i^{-n} S_n^{TM} h_n(k_b r) \left\{ \begin{array}{l} -\hat{\theta} \csc \theta p_n(\theta) \sin \varphi \\ -\hat{\phi} p_n'(\theta) \cos \varphi \end{array} \right\},$$

where $p_n(\theta) = P_n^1(\cos \theta)$ is the Legendre polynomial of first order, degree n and argument $\cos \theta$; in addition, h_n is the spherical Hankel function of order n and second type. The symbol $k_b = k_0 \sqrt{\epsilon_b} = 2\pi \sqrt{\epsilon_b} / \lambda$ stands for the wavenumber into the background medium and $\eta_0 = 120\pi \Omega$ the wave impedance into free space. The coefficients $S_n^{TE/TM}$, are complex dimensionless quantities and not shown here for brevity^{43,44}.

The power P_{scat} carried by the TE and TM scattered component, which constitutes a self-consistent electromagnetic field into the background host, expresses how much the sphere perturbs the background field distribution externally to it. It can be easily computed with use of Poynting's theorem and expansions of $h_n(k_b r)$ for large arguments $k_b r \gg 1$ (in the far region), as follows⁴⁵:

$$P_{scat} = P_0 \sum_{n=1}^{+\infty} \frac{n^2(n+1)^2}{2n+1} \left(|S_n^{TE}|^2 + |S_n^{TM}|^2 \right), \quad (4)$$

where $P_0 = \frac{\pi E_0^2}{k_0^2 \eta_0 \sqrt{\epsilon_b}} > 0$ is a quantity measured in *Watt* and k_0 is the free-space wavenumber. The power absorbed by the particle, given the presence of lossy constituent media, is evaluated by applying again Poynting's theorem but for the total field this time. Indeed, if we integrate the power spatial density across any sphere of radius $r > b$ (even the infinite $k_b r \rightarrow +\infty$ one), we obtain:

$$P_{abs} = -P_{scat} - P_0 \sum_{n=1}^{+\infty} n(n+1) \text{Re} [S_n^{TE} + S_n^{TM}]. \quad (5)$$

Obviously, $P_{scat}, P_{abs} > 0$, which means that the series in (5) should converge to negative values smaller than $(-P_{scat}/P_0)$. In the absence of any losses, we have $P_{abs} = 0$ and the aforementioned sum equals to $(-P_{scat}/P_0)$.

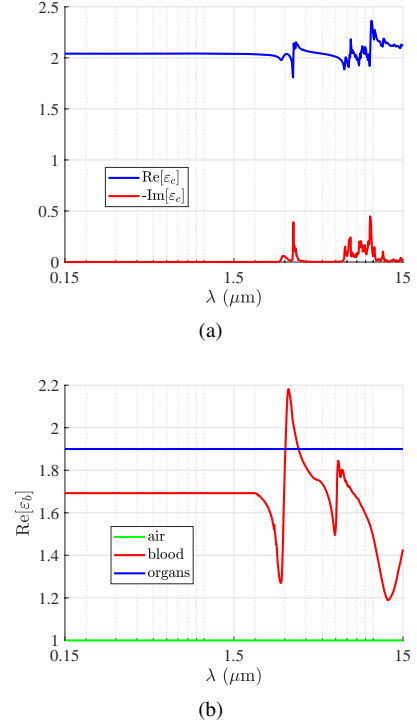


FIG. 2. Dispersive permittivities ϵ as functions of the incident wavelength λ . (a) Real and imaginary parts of the permittivity ϵ_c for protein (diisopropylamine, DIPA). The data is obtained from well-established source³¹ and expanded to short wavelength limit, based on lossless assumption⁴⁷. (b) Real parts of the background permittivity ϵ_b for alternative hosts: air, human blood and human organs (like liver). The various backgrounds are assumed to be lossless and the corresponding data has been obtained from reliable experimental measurements^{32,33}.

C. Parameters and Observables

Before proceeding to the numerical results and the discussion, let us first clarify the value ranges of the parameters incorporated into our model. In particular, the incident electromagnetic pulse is taken with a free-space central wavelength λ belonging to extensive band spanning from hard ultraviolet short waves ($\lambda = 150$ nm, UV-C) to long infrared radiation ($\lambda = 15$ μm , IR-C). In addition, we consider an external radius for the virion varying into the interval: $30 \text{ nm} < b < 100 \text{ nm}$, representing an assortment of various sizes¹⁹ and a radii ratio with $0.5 < a/b < 0.9$, corresponding to different lengths of the protein spikes⁴⁶. When it comes to the density s of the spikes, we regard all possible values: $0 < s < 1$ from an absent crown ($s = 0$) to a big homogeneous protein sphere of radius b ($s = 1$).

The variation for the dispersive permittivity for the homogeneous core $\epsilon_c = \epsilon_c(\lambda)$ is depicted in Fig. 2(a), where the data has been taken from reliable source³¹ and expanded to short wavelength limit⁴⁷. We notice that the regarded protein (diisopropylamine, DIPA) is lossless across large parts of the wavelength spectrum except for two bands around $\lambda \cong 3.5$ μm and $\lambda \cong 9.5$ μm ; these losses are responsible

for the corresponding variations of the real part $\text{Re}[\epsilon_c]$, according to the Kramers–Kronig relations that demand causal responses¹. As far as the permittivity of the host is concerned, it is lossless and non-dispersive for air and human organs like liver³³ as shown in Fig. 2(b). In the case of blood³², ϵ_b exhibits some variation accompanied by moderate losses that are ignored ($\text{Im}[\epsilon_b] = 0$) for a better formulation of the primary plane-wave excitation; otherwise a modification should be performed⁴⁸. Note that the real parts of the dielectric constants for the proteins, the human organs and the human blood are very close each other making a configuration of low textural contrast, where photonic power concentration is particularly challenging. Such a feature “pushed” us towards large operational frequencies (ultra-small wavelengths λ), as indicated above; only then the incoming light can interact strongly or resonate⁴⁹ with an inclusion constituting a so mild perturbation of the refractive index.

When it comes to the output of the system, we normalize the absorbed and scattered power by the power of the incident illumination passing through the geometrical cross section of the scatterer, namely $P_{inc} = \frac{\pi E_0^2 b^2 \sqrt{\epsilon_b}}{2\eta_0}$; in this way, the response of the virion becomes more meaningful. The most important quantity, however, is the extinction power $P_{ext} \equiv P_{scat} + P_{abs}$, namely the sum of scattering and absorption from (4),(5), so it represents the total effect of the particle on radiation traveling into the background medium; thus, the basic metric of our study is given by:

$$\frac{P_{ext}}{P_{inc}} = -\frac{2}{(k_0 b)^2 \epsilon_b} \sum_{n=1}^{+\infty} n(n+1) \text{Re} [S_n^{TE} + S_n^{TM}]. \quad (6)$$

The series (6) is rapidly converging once the optical size a/λ of the virion is small⁴¹, which is the case in the present formulation. Our aim will be to identify the conditions under which that ratio P_{ext}/P_{inc} is maximized so that the external electromagnetic beam couples optimally with the virion admitting its disintegration, conversion or neutralization.

III. RESULTS AND DISCUSSION

A. Maximal Extinction Power

In Fig. 3(a), we represent the extinction power P_{ext} normalized by the incident power P_{inc} with respect to the core-shell radii ratio a/b for the three different background media indicated by Fig. 2(b). We notice that the quantity showing how much the particle absorbs the radiation and “shakes” the local field distribution gets increased once the virion’s corona becomes thinner indicating a more substantial power concentration around the core. In addition, the beneficial influence of the material contrast between the spherical cell and the background on P_{ext}/P_{inc} can be identified since the highest values are recorded for airborne particles; on the contrary, the extinction power is small when $\epsilon_b \cong \epsilon_c$, as happening in the case of virions hosted into human organs. Quantitatively speaking, the magnitude P_{ext}/P_{inc} , at least for the adopted short wavelength ($\lambda \cong 250$ nm), is quite high and, for a densely pop-

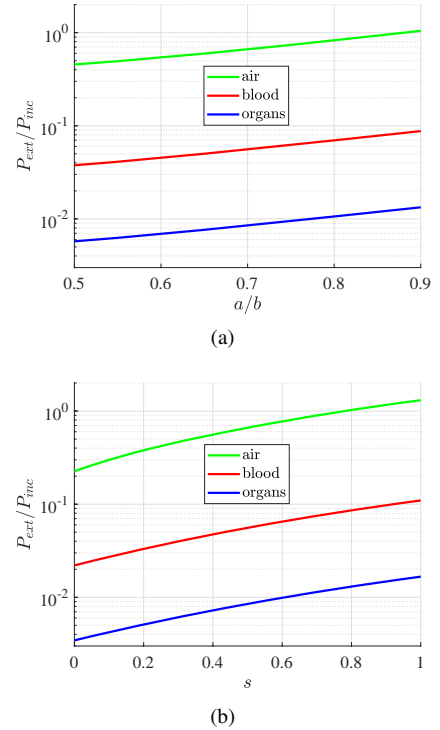


FIG. 3. The extinction power P_{ext} by the virion normalized by the incident power through the spherical cross section P_{inc} for various backgrounds ϵ_b , as a function of: (a) the core-shell radii ratio a/b ($s = 0.5$) and (b) the filling factor s of the shell ($a/b = 0.7$). Plot parameters: $\lambda = 250$ nm, $b = 80$ nm. The effect of the material contrast is identified.

ulated crown by protein spikes, it surpasses unity. In other words, the presence of particle participates in a huge power exchange with its environment concerning the whole electromagnetic radiation passing through its transection. Obviously a $P_{ext}/P_{inc} > 1$ is feasible since the object may interact with rays that are not directly incident on its spherical surface but travel in the vicinity of it⁵⁰.

In Fig. 3(b), we show the metric P_{ext}/P_{inc} from (6) as a function of the filling factor s for alternative hosts. A rapidly increasing trend is observed, demonstrating once more the amplifying effect of the needle-shaped rods on the particle-beam interaction. Furthermore, the textural contrast is again recognized as a factor that boosts the extinction power, while the measured quantity is somehow higher compared to Fig. 3(a). It is also noticed that, despite the low difference between the refractive index of blood and organs as shown in Fig. 2(b), the corresponding extinction power in human blood background is much higher; indeed, what counts is the spread between ϵ_b and the protein’s permittivity ϵ_c as depicted in Fig. 2(a).

Given the fact that Fig. 3 concerns the interplay of the particle with the incoming illumination at ultra-violet frequencies, it is important to understand the response of the spherical virion across the whole of the considered band. In particular, in Fig. 4(a), we represent the variation of the ratio P_{ext}/P_{inc} with respect to oscillation wavelength λ for the three

regarded hosts. When the wavelengths are tiny ($\lambda < 1 \mu\text{m}$), it is natural to spot a declining trend since the particle is not optically big enough to interact substantially with the incident electromagnetic pulse. However, beyond $1.5 \mu\text{m}$, where proteins exhibit significant losses (see Fig. 2(a)), the metric increases by orders of magnitudes to reach a strong local maximum at $\lambda \cong 3.37 \mu\text{m}$, regardless of the background. Therefore, in order to maximally engage with that specific type of corona-virions, one should concentrate the impinging power in the spectral vicinity of that frequency; this conclusion is one of the major findings of our study. Similar resonances are exploited for protein molecule monolayers detection by covering the sensor to produce a controllable amount of resonance redshift⁵¹. It should be finally stressed that the results are host-indifferent only when the operating wavelengths λ are large enough; for $\lambda < 1 \mu\text{m}$, the relative order of P_{ext}/P_{inc} for different hosts is dictated by the material contrast of Fig. 2, as happening in Fig. 3.

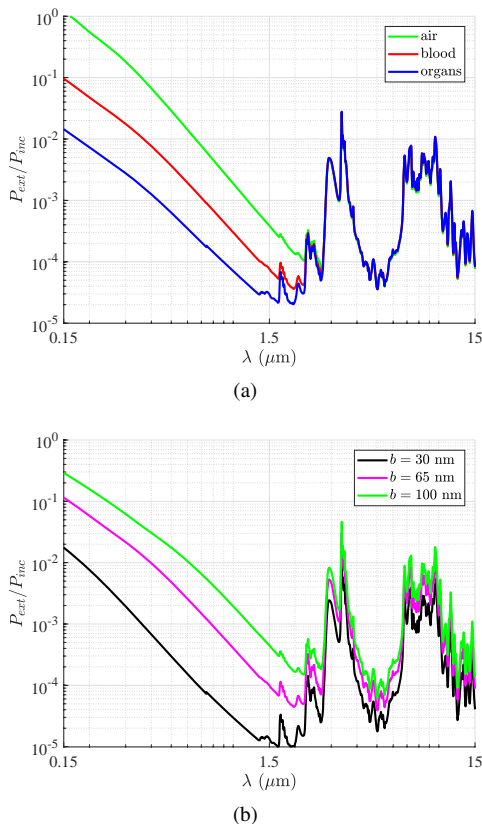


FIG. 4. The extinction power P_{ext} by the virion normalized by the incident power through the spherical cross section P_{inc} as a function of the incoming wavelength λ for: (a) various host environments ϵ_b ($b = 60 \text{ nm}$), (b) various external sizes b of the virions (in blood). Plot parameters: $a/b = 0.7$, $s = 0.5$. The strong local optimum at mid-infrared ($\lambda \cong 3370 \text{ nm}$) is spotted, regardless of background and size.

In Fig. 4(b), we repeat the calculations of Fig. 4(a) but for different sizes of virions b , all existing into human blood. The variation of P_{ext}/P_{inc} is similar to that of Fig. 4(a) but the larger size makes a difference and increases, on average, the

represented metric, even at lower frequencies ($\lambda > 1.5 \mu\text{m}$). However, the major maximum at $\lambda \cong 3.37 \mu\text{m}$ discussed above, is present no matter how small is the virion and, importantly, it gives almost the same relative extinction power. Such a feature remarks further the significance of the reported resonance, since the electromagnetic beam concentrated around a single wavelength allows for maximal interplay with an ensemble of virus particles possessing various sizes. Note that mid-infrared frequency range makes a privileged band for biosensing⁵² and chemical identification of biomolecules through their vibrational fingerprints, namely, photonic operation at this resonance is experimentally feasible⁵³.

B. Power Spatial Distribution

After having understood the influence of structural (a/b , s), textural (several background) and spectral (λ) parameters on the way that corona-virions interact with the incident beams, it would be meaningful to show the spatial distribution of electromagnetic power inside and outside the core-shell particle for characteristic cases. In Fig. 5(a), we show the relative field quantity $|\mathbf{E}/E_0|^2$ across zx plane, when the structure is excited at the optimal mid-infrared wavelength ($\lambda \cong 3.37 \mu\text{m}$) into human blood host; the represented quantity may be discontinuous as one crosses an interface between two different media, due to the change in texture. By inspection of Fig. 5(a), one directly notices that the values of the electric field magnitude $|\mathbf{E}|$ are very close to that of the incident plane wave E_0 ; however, it is natural given the very low permittivity contrast of the virion with its environment. On the contrary, the power concentration at the interior of the spherical volume is counter-intuitive and noteworthy since it clearly demonstrates the substantial interaction of the entire virion with the incoming pulse. As recently reported⁵⁴, such a physical focus of light is useful to photomedicine while can be directly utilized for thermal damage in biological applications. That significant property is also illustrated when the zy plane is considered (Fig. 5(b)) but the distribution is not identical to that of Fig. 5(a) due to the vectorial nature of the incident plane wave which is polarized along x axis.

To show that the bright spots of Figs 5(a),5(b) are not easily achieved, in Figs 5(c),5(d) we show the distribution of $|\mathbf{E}/E_0|^2$ when the incoming wavelength is arbitrarily picked ($\lambda = 2.2 \mu\text{m}$). Despite the fact that the pulse is faster making the virion look larger and admitting it to develop more complex dynamics, the field into the object is lower than the background level forming a bipolar pattern; as a result, the ability of the primary excitation to engage with the particle is severely diminished compared to the optimal case of Fig. 5(a). Similar conclusions can be drawn by juxtaposing Figs 5(c),5(d) referring to zy plane; in the scenario of randomly selected wavelength, the pattern is omni-directional and the power is weak into the scatterer, contrary to the signal focusing exhibited in Fig. 5(d).

In Fig. 6, higher frequencies are examined; more specifically, in Fig. 6(a) we show the electric field across zx plane under violet color illumination ($\lambda = 350 \text{ nm}$). One directly notices that the field is stronger at the rear side of the virion

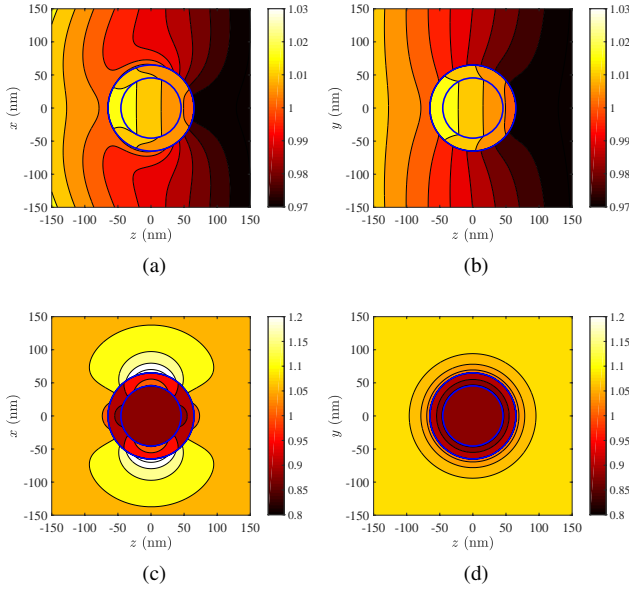


FIG. 5. Spatial distribution of the total electric field $|\mathbf{E}/E_0|^2$ across xz and zy planes when the incoming pulse travels along $+z$ axis for: (a,b) $\lambda = 3370$ nm (optimal mid-infrared wavelength) (c,d) $\lambda = 2200$ nm (arbitrary smaller wavelength). Plot parameters: $a/b = 0.7$, $s = 0.5$, $b = 65$ nm, human blood background. The blue lines indicate the boundaries between two different media.

but, if an averaging is performed, the relative signal within the volume of the particle is comparable to that of Fig. 5(a), even though the incident wavelength is ten times smaller and much less harmful for the surroundings (healthy cells, tissues, organs) into human body. It is also found that the field increases along z axis into the homogeneous core, contrary to what is happening to Figs 5(a),5(b), where the opposite trend is recorded. In Fig. 6(b), a larger wavelength corresponding to red color ($\lambda = 700$ nm) is assumed; we observe a substantially poorer relative power concentration compared to both Figs 5(a),6(a) for a much faster pulse than the one operated at the optimal regime.

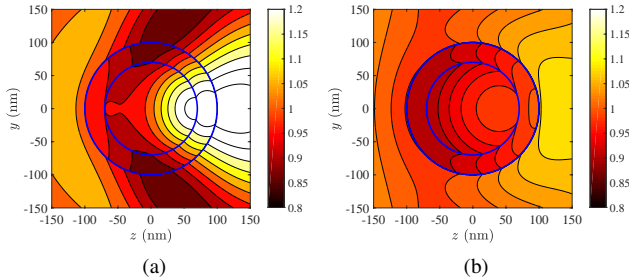


FIG. 6. Field concentration at shorter wavelengths. Spatial distribution of the total electric field $|\mathbf{E}/E_0|^2$ across zy plane when the incoming pulse travels along $+z$ axis for: (a) $\lambda = 350$ nm, (b) $\lambda = 700$ nm. Plot parameters: $a/b = 0.7$, $s = 0.5$, $b = 100$ nm, human blood background. The blue lines indicate the boundaries between two different media.

In Fig. 7, we examine the effect of the radii ratio a/b on the spatial distribution of the electric field $|\mathbf{E}/E_0|^2$, when working close to the reported optimal point ($\lambda \cong 3.37 \mu\text{m}$). It is apparent that the power accumulation is significant in all the considered cases and gets higher for an increasing a/b , as also indicated by Fig. 3(a). In the same way that Fig. 4(b) shows insensitivity of the identified effect from the viral size b , Fig. 7 designates that the resonance is practically indifferent to the corona thickness ($b - a$) and thus a universal effectiveness against large families of virions possessing diverse characteristics, is demonstrated. Such an optical trap allows for manipulation and energy exchange with individual viral nanoparticles that can lead to their disintegration or neutralization; similar biomagnifying effects are reported for different applications⁵⁵ like optical imaging and assembly of bionanomaterials. The experimental potential of the described effect is further underlined by the fact that this type of resonances make typical spectrophotometers to be sensitive in the activity of individual enzymes; thus, it renders the device suitable⁵⁶ for on-chip antibody or antigen detection and chromogenic-based operations such as bacteria detection.

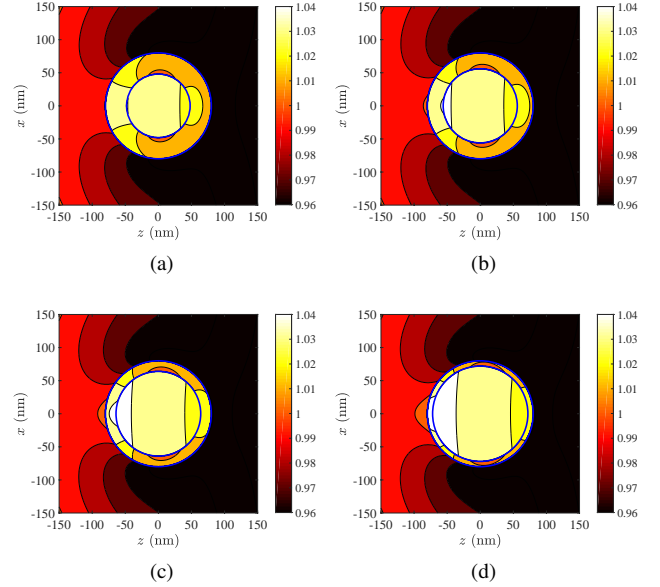


FIG. 7. Effect of aspect ratio on the field concentration at optimal mid-infrared wavelength. Spatial distribution of the total electric field $|\mathbf{E}/E_0|^2$ across xz plane when the incoming pulse travels along $+z$ axis for: (a) $a/b = 0.6$, (b) $a/b = 0.7$, (c) $a/b = 0.8$, (d) $a/b = 0.9$. Plot parameters: $s = 0.6$, $b = 80$ nm, $\lambda = 3367$ nm, human blood background.

IV. CONCLUDING REMARK

A single corona virion is modeled as a homogeneous spherical core surrounded by a conformal isotropic shell, under illumination from electromagnetic pulses. Rigorous Mie theory is applied to obtain the analytical solution of the formulated boundary value problem and compute the total extinction

power of the particle. This quantity indicates how successfully the considered cells interacts with the incoming fields and is found to be maximal at a specific mid-infrared resonance that is independent from the structural characteristics or the background host. A substantial power exchange between impinging beams and the object is necessary for a series of actions dealing with the virion from thermal damage and dissolution to neutralization and isolation; therefore, the reported findings may pave the way to more efficient radiation treatments against SARS-CoV-2.

The proposed model can be refined to include anisotropic multilayers both at the core for more detailed description of the engulfed genome and at the shell to take into account the radial distribution of the protein spikes. Such a process will involve complex-ordered Bessel functions calling for careful computation⁴¹; similarly, alternative excitation beams or time-restricted causal pulses instead of plane waves can be taken into account by properly evaluating complex Fourier integrals⁵⁷. Importantly, an interesting follow-up of our approach would be to regard clusters of cells and investigate their collective dynamics by implementing suitable transforms for the summation^{58,59} of the responses from randomly or deterministically placed cells⁶⁰. In this way, the work at hand can be considered as the first step towards the successful modeling of corona-virions and the derivation of analytical formulas for the exchanged power which will simplify significantly the subsequent optimizations and make easier the designation of optimal operation regimes.

ACKNOWLEDGMENTS

This work was partially supported by Nazarbayev University Grant No. 090118FD5349 entitled: “Super transmitters, radiators and lenses via photonic synthetic matter”. Funding from MES RK state-targeted program BR05236454 is also acknowledged.

The data that supports the findings of this study are available within the article.

- ¹C. F. Bohren and D. R. Huffman, *Absorption and Scattering of Light by Small Particles*, Wiley-VCH, 1998.
- ²S. E. Harding, *Microbial Laser Light Scattering*, Biotechnol. Genet. Eng. **14**, 145 (1997).
- ³W. J. Kowalski, *Ultraviolet Germicidal Irradiation Handbook*, Springer, 2009.
- ⁴S. E. Harding, *Applications of Light Scattering in Microbiology*, Biotechnol. Appl. Biochem. **8**, 489 (1986).
- ⁵J. Stetefeld, S. A. McKenna, and T. R. Patel, Dynamic light scattering: a practical guide and applications in biomedical sciences, *Biophys. Rev.* **8**, 409 (2016).
- ⁶T. Yoshikawa, M. Tamura, S. Tokonami, and T. Iida, Optical Trap-Mediated High-Sensitivity Nanohole Array Biosensors with Random Nanospikes, *J. Phys. Chem. Lett.* **8**, 370 (2017).
- ⁷F. Vollmer, S. Arnold, and D. Keng, Single virus detection from the reactive shift of a whispering-gallery mode, *Proc. Nat. Acad. Sci. USA* **105**, 20701 (2008).
- ⁸Y. Pang, H. Song, and W. Cheng, Using optical trap to measure the refractive index of a single animal virus in culture fluid with high precision, *Biomed. Opt. Express* **7**, 257675 (2016).
- ⁹L. Ma, S. Zhu, Y. Tian, W. Zhang, S. Wang, C. Chen, L. Wu, and X. Yan, Label-Free Analysis of Single Viruses with a Resolution Comparable

- to That of Electron Microscopy and the Throughput of Flow Cytometry, *Angew. Chem. Int. Ed.* **55**, 10239 (2016).
- ¹⁰H. C. van de Hulst, *Light Scattering by Small Particles*, Dover, 1981.
- ¹¹D. J. Gordon and G. Holzwarth, Optical Activity of Membrane Suspensions: Calculation of Artifacts by Mie Scattering Theory, *Proc. Nat. Acad. Sci. USA* **68**, 2365 (1971).
- ¹²W. M. Balch, J. Vaughn, J. Novotny, D. T. Drapeau, R. Vaillancourt, J. Lapiere, and A. Ashe, Light scattering by viral suspensions, *Limnol. Oceanogr.* **45**, 492 (2000).
- ¹³R. Yan, N. S. Lynn, L. C. Kingry, Z. Yi, T. Erickson, R. A. Slayden, D. S. Dandy, and K. L. Lear, Detection of virus-like nanoparticles via scattering using a chip-scale optical biosensor, *Appl. Phys. Lett.* **101**, 161111 (2012).
- ¹⁴G. Brittain, S. Gulnik, and Y. Chen, Characterizing the Light-Scatter Sensitivity of the CytoFLEX Flow Cytometer, Poster by Beckman Coulter Life Sciences, Miami, FL 33196. Online available: here.
- ¹⁵Z. A. Steelman, W. J. Eldridge, J. B. Weintraub, and A. Wax, Is the nuclear refractive index lower than cytoplasm? Validation of phase measurements and implications for light scattering technologies *J. Biophotonics* **10**, 1714 (2017).
- ¹⁶M. R. Foreman, and F. Vollmer, Theory of resonance shifts of whispering gallery modes by arbitrary plasmonic nanoparticles, *New J. Phys.* **15**, 083006 (2013).
- ¹⁷M. A. Santiago-Cordoba, M. Cetinkaya, S. V. Boriskina, F. Vollmer, and M. C. Demirel, Ultrasensitive Detection of a Protein by Optical Trapping in a Photonic-Plasmonic Microcavity, *J. Biophotonics* **5**, 629 (2012).
- ¹⁸F. Wu *et al.*, A new coronavirus associated with human respiratory disease in China, *Nature* **579**, 265 (2020).
- ¹⁹N. Zhu *et al.*, A Novel Coronavirus from Patients with Pneumonia in China, 2019, *N. Engl. J. Med.* **382**, 727 (2020).
- ²⁰L. Corey, J. R. Mascola, A. S. Fauci, and F. S. Collins, A strategic approach to COVID-19 vaccine R&D, *Science* **368**, 948 (2020).
- ²¹Guangyu Qiu, Zhibo Gai, Yile Tao, J. Schmitt, G. A. Kullak-Ublick, and J. Wang, Dual-Functional Plasmonic Photothermal Biosensors for Highly Accurate Severe Acute Respiratory Syndrome Coronavirus 2 Detection, *ACS Nano* **14**, 5268 (2020).
- ²²Q. Zhang, A. Honko, J. Zhou, H. Gong, S. N. Downs, J. H. Vasquez, R. H. Fang, W. Gao, A. Griffiths, and L. Zhang, Cellular Nanosponges Inhibit SARS-CoV-2 Infectivity, *Nano Lett.*, Accepted for Publication (2020).
- ²³C. S. Enwemeka, V. V. Bumaha, and D. S. Masson-Meyers, Light as a potential treatment for pandemic coronavirus infections: A perspective, *J. Photoch. Photobiol. B* **207**, 111891 (2020).
- ²⁴D. Petrov, Photopolarimetric properties of coronavirus model particles: spike proteins number influence, *J. Quant. Spectrosc. Radiat. Transf.* **248**, 107005 (2020).
- ²⁵Q. Ye, A. M.V. West, S. Silletti, K. D. Corbett, Architecture and self-assembly of the SARS-CoV-2 nucleocapsid protein, Uploaded at BioRxiv, Online available here (2020).
- ²⁶F. Li, Structure, Function, and Evolution of Coronavirus Spike Proteins, *Annu. Rev. Virol.* **3**, 237 (2016).
- ²⁷B. J. Bosch, R. van der Zee, C. A. M. de Haan, and P. J. M. Rottier, The Coronavirus Spike Protein Is a Class I Virus Fusion Protein: Structural and Functional Characterization of the Fusion Core Complex, *J. Virol.* **77**, 8801 (2003).
- ²⁸V. Stadnytskyi, C. E. Bax, A. Bax, and P. Anfinrud, The airborne lifetime of small speech droplets and their potential importance in SARS-CoV-2 transmission, *Proc. Nat. Acad. Sci. USA* **117**, 11875 (2020).
- ²⁹L. Chang, Y. Yan, and L. Wang, Coronavirus Disease 2019: Coronaviruses and Blood Safety, *Transfus. Med. Rev.* **34**, 75 (2020).
- ³⁰L. Xu, J. Liu, M. Lu, D. Yang, and X. Zheng, Liver injury during highly pathogenic human coronavirus infections, *Liver Int.* **40**, 998 (2020).
- ³¹T. L. Myers, R. G. Tonkyn, T. O. Danby, M. S. Taubman, B. E. Bernacki, J. C. Birnbaum, S. W. Sharpe, and T. J. Johnson, Accurate Measurement of the Optical Constants n and k for a Series of 57 Inorganic and Organic Liquids for Optical Modeling and Detection, *Appl. Spectrosc.* **72**, 535 (2018).
- ³²D. J. Rowe, D. Smith, and J. S. Wilkinson, Complex refractive index spectra of whole blood and aqueous solutions of anticoagulants, analgesics and buffers in the mid-infrared, *Sci. Rep.* **7**, 7356 (2017).
- ³³P. Giannios, K. G. Toutouzas, M. Matiatou, K. Stasinou, M. M. Konstadoulakis, G. C. Zografos, and K. Moutzouris, Visible to near-infrared refractive properties of freshly-excised human-liver tissues: marking hepatic

- malignancies, *Sci. Rep.* **6**, 27910 (2016).
- ³⁴A. C. Walls, Y.-J. Park, M. A. Tortorici, A. Wall, A. T. McGuire, and D. Veessler, Structure, Function, and Antigenicity of the SARS-CoV-2 Spike Glycoprotein, *Cell* **180**, 281 (2020).
- ³⁵C. A. Valagiannopoulos and N. L. Tsitsas, Linearization of the T-matrix solution for quasi-homogeneous scatterers, *J. Opt. Soc. Am. A* **26**, 870 (2009).
- ³⁶F. Mangini, N. Tedeschi, F. Frezza, and A. Sihvola, Homogenization of a multilayer sphere as a radial uniaxial sphere: features and limits, *J. Electromagn. Waves Appl.* **28**, 916 (2014).
- ³⁷H. Wallén, H. Kettunen, and A. Sihvola, Anomalous absorption, plasmonic resonances, and invisibility of radially anisotropic spheres, *Radio Sci.* **50**, 28 (2015).
- ³⁸T. Rimpilainen, H. Wallén, H. Kettunen, and A. Sihvola, Electrical response of sypstropic sphere, *IEEE Trans. Antennas Propag.* **60**, 5348 (2012).
- ³⁹A. Sihvola, *Electromagnetic Mixing Formulas and Applications*, IET, 1999.
- ⁴⁰L. Gao, T. H. Fung, K. W. Yu, and C. W. Qiu, Electromagnetic transparency by coated spheres with radial anisotropy, *Phys. Rev. E* **78**, 046609 (2008).
- ⁴¹C. A. Valagiannopoulos, An overview of the Watson transformation presented through a simple example, *Electromagn. Waves (Camb.)* **75**, 137 (2007).
- ⁴²A. Sheverdin and C. Valagiannopoulos, Core-shell nanospheres under visible light: Optimal absorption, scattering, and cloaking, *Phys. Rev. B* **99**, 075305 (2019).
- ⁴³A. Alù and N. Engheta, Achieving transparency with plasmonic and metamaterial coatings, *Phys. Rev. E* **72**, 016623 (2005).
- ⁴⁴C. Valagiannopoulos, Maximal quantum scattering by homogeneous spherical inclusions, *Phys. Rev. B* **100**, 035308 (2019).
- ⁴⁵C. A. Valagiannopoulos, Single-series solution to the radiation of loop antenna in the presence of a conducting sphere, *Electromagn. Waves (Camb.)* **71**, 277 (2007).
- ⁴⁶K. H. J. Buschow, *Encyclopedia of Materials: Science and Technology*, Elsevier, 1998.
- ⁴⁷M. Jonasz and G. R. Fournier, *Light Scattering by Particles in Water*, Elsevier, 2011.
- ⁴⁸Q. Fu and W. Sun, Mie theory for light scattering by a spherical particle in an absorbing medium, *Appl. Opt.* **40**, 1354 (2001).
- ⁴⁹D. C. Tzarouchis and A. Sihvola, General Scattering Characteristics of Resonant Core-Shell Spheres, *IEEE Trans. Antennas Propag.* **66**, 323 (2018).
- ⁵⁰C. A. Valagiannopoulos, J. Vehmas, C. R. Simovski, S. A. Tretyakov, and S. I. Maslovski, Electromagnetic energy sink, *Phys. Rev. B* **92**, 245402 (2015).
- ⁵¹M. Lee and P. M. Fauchet, Two-dimensional silicon photonic crystal based biosensing platform for protein detection, *Opt. Express* **15**, 4530 (2007).
- ⁵²M. Dubrovsky, M. Blevins, S. V. Boriskina, and D. Vermeulen, High Contrast Probe Cleavage Detection, Submitted to ResearchGate, DOI: 10.13140/RG.2.2.24831.23201, (2020).
- ⁵³D. Rodrigo, O. Limaj, D. Janner, D. Etezadi, F. J. G. de Abajo, V. Pruneri, and H. Altug, Mid-infrared plasmonic biosensing with graphene, *Science* **349**, 165 (2015).
- ⁵⁴E. Edrei and G. Scarcelli, Optical Focusing beyond the Diffraction Limit via Vortex-Assisted Transient Microlenses, *ACS Photonics* **7**, 914 (2020).
- ⁵⁵Y. Li, X. Liu, and B. Li, Single-cell biomagnifier for optical nanoscopes and nanotweezers, *Light Sci. Appl.* **8**, 61 (2019).
- ⁵⁶A. Nitkowski, A. Baeumner, and M. Lipson, On-chip spectrophotometry for bioanalysis using microring resonators *Opt. Express* **2**, 271 (2011).
- ⁵⁷H. J. A. da Silva and J. J. O'Reilly, Optical pulse modeling with Hermite-Gaussian functions, *Opt. Lett.* **14**, 526 (1989).
- ⁵⁸S.-Z. Lin, Y. Li, J. Ji, B. Li, and X.-Q. Feng, Collective dynamics of coherent motile cells on curved surfaces, *Soft Matter* **16**, 2941 (2020).
- ⁵⁹Z. Tagay and C. Valagiannopoulos, Highly selective transmission and absorption from metasurfaces of periodically corrugated cylindrical particles, *Phys. Rev. B* **98**, 115306 (2018).
- ⁶⁰A. Monti, A. Alù, A. Toscano, and F. Bilotti, Surface Impedance Modeling of All-Dielectric Metasurfaces, *IEEE Trans. Antennas Propag.* **68**, 1799 (2020).